ACS APPLIED MATERIALS & INTERFACES

www.acsami.org Research Article

Visualizing and Controlling of Photogenerated Electron−Hole Pair Separation in Monolayer WS_2 Nanobubbles under Piezoelectric Field

Sheng Han,[¶] Jiong Liu,[¶] Ana I. Pérez-Jiménez, Zhou Lei, Pei Yan, Yu Zhang, Xiangyu Guo, Rongxu Bai, Shen Hu,* Xuefeng Wu,* David W. Zhang, Qingqing Sun, Deji Akinwande, Edward T. Yu,* and Li Ji*

Cite This: *ACS Appl. Mater. Interfaces* 2024, 16, 36735−36744 Read Online

ACCESS | Metrics & More | Article Recommendations | Supporting Information

ABSTRACT: The piezoelectric properties of two-dimensional semiconductor nanobubbles present remarkable potential for application in flexible optoelectronic devices, and the piezoelectric field has emerged as an efficacious pathway for both the separation and migration of photogenerated electron−hole pairs, along with inhibition of recombination. However, the comprehension and control of photogenerated carrier dynamics within nanobubbles still remain inadequate. Hence, this study is dedicated to underscore the importance of *in situ* detection and detailed characterization of photogenerated electron−hole pairs in nanobubbles to enrich understanding and strategic manipulation in two-dimensional semiconductor materials. Utilizing frequency modulation kelvin probe force microscopy (FM-KPFM) and strain gradient distribution techniques, the existence of a piezoelectric field in monolayer WS_2 nanobubbles was confirmed. Combining w/o and with illumination FM-KPFM, second-order capacitance gradient technique and *in situ* nanoscale tip-enhanced photoluminescence characterization techniques, the interrelationships among the piezoelectric effect, interlayer carrier transfer, and the funneling effect for photocarrier dynamics process across various nanobubble sizes were revealed. Notably, for a WS_2/graphene bubble height of 15.45 nm, a 0 mV surface potential difference was recorded in the bubble region w/o and with illumination, indicating a mutual offset of piezoelectric effect, interlayer carrier transfer, and the funneling effect. This phenomenon is prevalent in transition metal dichalcogenides materials exhibiting inversion symmetry breaking. The implication of our study is profound for advancing the understanding of the dynamics of photogenerated electron−hole pair in nonuniform strain piezoelectric systems, and offers a reliable framework for the separation and modulation of photogenerated electron−hole pair in flexible optoelectronic devices and photocatalytic applications.

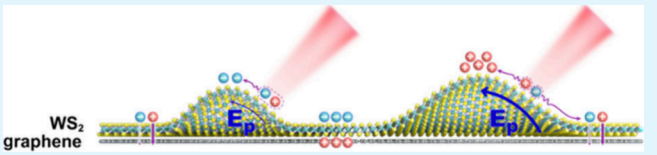

KEYWORDS: *WS_2 Nanobubbles, FM-KPFM, TEPL, Photogenerated electron−hole separation, Piezoelectric field, Funneling effect, in situ*

INTRODUCTION

Transition metal dichalcogenides (TMDCs), with the chemical formula MX_2 (M = transition metals and X = S, Se, Te), possess tunable bandgap structures, excellent light absorption rates, relatively high carrier mobility,[1] strong light−matter interaction, broadband light absorption and high on/off ratios, making them ideal for ultrathin flexible optoelectronic applications including light-emitting diodes,[2−4] photodetectors,[5−8] solar cells,[9−11] and photocatalysis.[12,13] The carrier dynamics of TMDCs, encompassing processes like generation, separation, recombination, and transport,[14] exerts a pivotal influence on the operation of ultrathin flexible optoelectronic devices. However, in TMDCs, carriers are primarily confined to a two-dimensional (2D) plane, resulting in enhanced Coulomb interaction and reduced dielectric screening, leading to the recombination of photogenerated electron−hole pairs, thus inhibiting the generation of photocurrent. Therefore, there is an immediate and compelling necessity to effectively separate photogenerated electron−hole pairs to improve the photoelectric characteristics of the TMDCs device. Various approaches have been tried by researchers, for example, heterostructure engineering,[15,16] defect engineering[17−19] and strain engineering.[20,21]

Notably, the remarkable mechanical flexibility (strain up to 10%) of 2D materials opens up intriguing possibilities for conveniently modulating the electronic and optical properties by strain engineering. Numerous interesting effects have been predicted and observed through the bending and stretching of 2D materials.[22−25] In particular, nanobubbles have sparked intense research interest because of facile fabrication, strong strain adjustability, and persistent mechanical strain without applying external forces. Nanobubbles can spontaneously manifest, encapsulating air, liquids, or hydrocarbons in the

Received: January 2, 2024
Revised: June 19, 2024
Accepted: June 23, 2024
Published: July 2, 2024

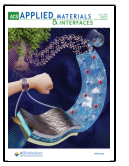

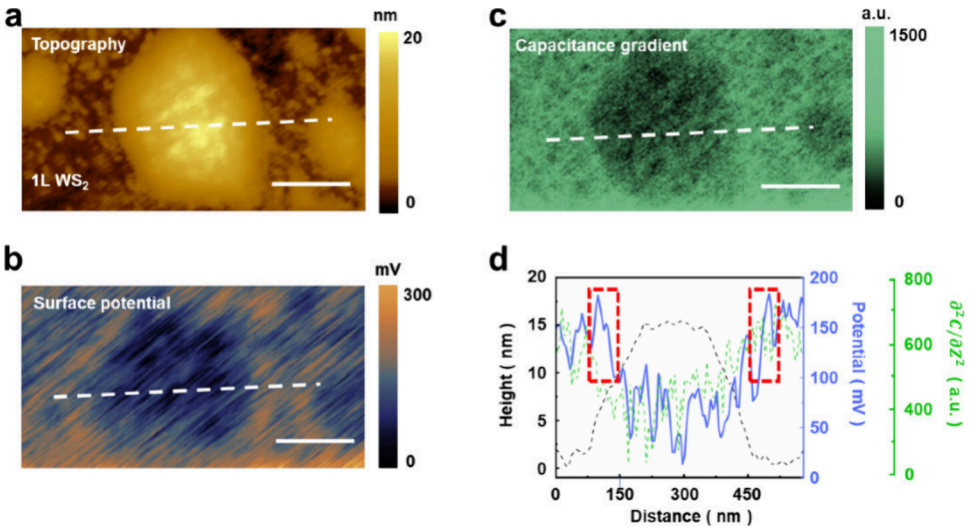

Figure 1. Topography and electrical characterization of monolayer WS_2 bubbles on Si/SiO_2 substrate. (a) AFM topography measurements on monolayer WS_2 bubbles. (b) FM-KPFM measurements on monolayer WS_2 bubbles. (c) Capacitance gradient measurements on monolayer WS_2 bubbles. (d) Height, relative SP and $\partial^2C/\partial z^2$ profiles along the white dashed lines in (a), (b), and (c) panels. The red-dashed squares highlight a sharp increase of the SP value around the bubble edge. All scale bars, 200 nm. The pixel size is 3.89 × 3.89 nm^2.

pockets squeezed between adjacent layers owing to the competition between van der Waals (vdW) forces and elastic energy. Recent experiments and simulations have revealed that enormous local strain occurring in and around bubbles can induce a unique piezoelectric field distribution in the bubble region of 2D crystals that lack symmetric inversion especially for hexagonal boron nitride (hBN) and TMDCs with odd numbers of layers.[26,27] Similarly, flexoelectric effects can be prominent in atomically thin TMDCs due to the large and highly inhomogeneous strain fields that can be present.[28,29] The existence of piezoelectric and/or flexoelectric polarization fields provides an intriguing possibility for the efficient separation of the photogenerated electron−hole pair in TMDCs nanobubbles.

In situ nanoscale characterization of photogenerated electron−hole pairs is imperative to enhance the comprehension and facilitate efficient regulation of charge carrier separation in TMDCs nanobubbles. The frequency modulation kelvin probe force microscope (FM-KPFM) technique has been employed to visualize and quantitatively detect the surface potential (SP), or the localized potential variation, in TMDCs materials along the strain direction due to the piezoelectric effect.[30] However, within the TMDCs bubble system, the strain-induced band narrowing causes the photogenerated electrons and holes to move toward the top of the bubble since tensile strain reaches a maximum at that point, that is, the funneling effect,[31−34] which has a significant influence on the overall distribution of photogenerated electron−hole pairs and the SP results detected by FM-KPFM. Experiments to date, however, have yet to distinctly delineate these two regulation mechanisms or to yield quantitative results of piezoelectric potential and strain-induced funneling effect on photogenerated carrier dynamics within the nanobubble system at the desired nanoscale resolution. Therefore, a comprehensive technique that can obtain localized strain, piezoelectric potential, and *in situ* illuminance mapping signals is needed to obtain a more precise understanding of photogenerated carrier dynamics within nanoscale TMDCs bubble systems or other analogous strain systems to help design specific structures that effectively regulate photogenerated carrier dynamic processes.

In this study, a nonuniform strain system was engineered with monolayer WS_2 nanobubbles on Si/SiO_2 and graphene. Utilizing FM-KPFM combined with a strain gradient distribution, the piezoelectric coefficient of monolayer WS_2 was determined. Meanwhile, the SP difference between the w/o and with illumination were visualized. Nanoscale *in situ* characterization techniques including FM-KPFM and tip-enhanced photoluminescence (TEPL) were harnessed to compare the results at various bubble heights for investigating the correlation between nanoscale photogeneration electron−hole pairs separation and bubble sizes. Moreover, the complementary gain and competitive effects deduced by the piezoelectric effect, the interlayer carrier transfer[35−38] and the funneling effect for photocarrier dynamics process at diverse nanobubbles heights were elucidated. We basically separate the regulation rules of piezoelectric potential and the strain-induced funneling effect on photogenerated carriers and the relative quantitative results under the nanobubble system. This research holds substantial importance for the enhanced understanding on the photoexcited carrier dynamics of nonuniform strain piezoelectric systems and provides a reliable method for the segregation and control of photogenerated electron−hole pairs, aiming to bolster the efficacy of 2D flexible optoelectronic devices.

RESULTS AND DISCUSSION

For hexagonal structures that belong to the D_6h point group, such as WS_2 and WSe_2, a reduction in symmetry to the D_3h group is observed for monolayers, in which the inversion symmetry of bulk crystals is broken.[39] To substantiate this concept, we verified the existence of the piezoelectric field in the monolayer WS_2 bubble region. We transferred monolayer WS_2 on the Si/SiO_2 substrate by a dry-transfer technique, and bubbles spontaneously shape randomly due to the filling of hydrocarbons or gases between the WS_2 and Si/SiO_2 (see the Methods). Since SiO_2 is not a lipophilic surface and does not have a self-cleaning effect, the distribution of WS_2 bubbles is

https://doi.org/10.1021/acsami.4c00092
ACS Appl. Mater. Interfaces 2024, 16, 36735−36744

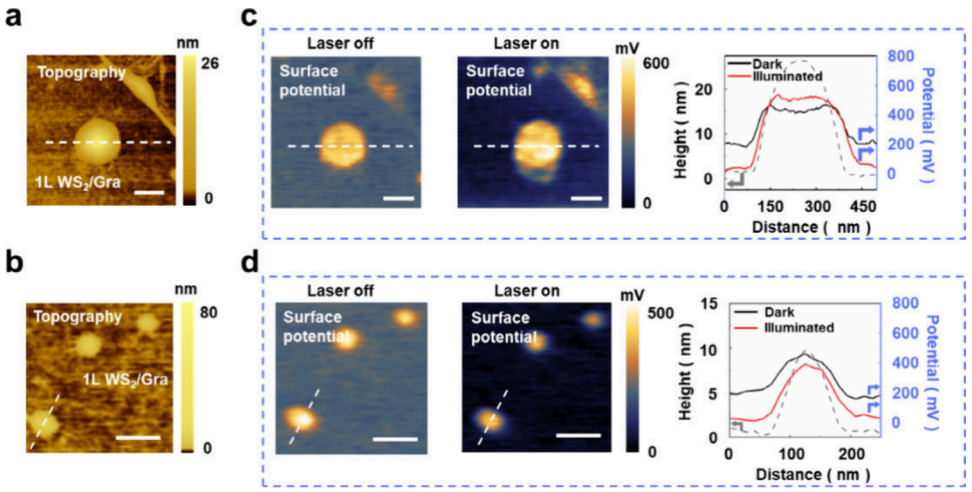

Figure 2. Comparison of surface potential variations w/oand with illumination of the monolayer WS_2 bubbles on monolayer graphene. (a, b) AFM topography measurements of the large WS_2 bubbles on monolayer graphene (a), and the pocket ones (b), respectively. (c, d) FM-KPFM measurements of the large WS_2 bubbles on monolayer graphene (a) for (c) and the pocket ones (b) for (d), respectively. Profile of height, relative potential w/o, and with illumination along the white dashed lines in (a, b) and in the left and middle panels of (c, d), respectively. All scale bars, 200 nm. The pixel size is 3.89 × 3.89 nm^2 for the large WS_2/graphene bubbles (a) and 11.68 × 11.68 nm^2 for the pocket ones (b). The laser power is 0.2 mW.

usually dense. In order to avoid the influence of surrounding bubbles on the intrinsic bubble properties, we chose the typical bubbles with relatively flat surroundings for exploration. h/R (where h is the maximum height and R is the radius of the bubble) is a parameter used to define the morphology of the bubbles. According to previous reports, it is worth mentioning that the h/R value of bubbles is basically constant under the same 2D crystal/substrate combination, independent of the bubble size.[40−42] There are only two characteristic variables that determine the h/R value of the heterostructure bubbles: in-plane stiffness (Young's modulus Y) of the upper monolayer and its adhesion energy γ to the substrate. The theory leads to the following general formula $h/R = (\pi\gamma/5c_1Y)^{1/4}$, where the numerical coefficient $c_1 \approx 0.7$.[40−42]

Figure 1a shows the topography of the WS_2 bubble, as characterized by atomic force microscopy (AFM) operating in the tapping mode. The bubbles' height, SP and second-order capacitance gradient (CG) curve along the white dotted line are shown in Figure 1d, with a maximum bubble height of 13.1 nm. Due to the irregular shape of bubbles, we perform a normative processing according to the circular model and choose four directions to obtain the equivalent average value; the radius is 187.1 nm, and the h/R value of the WS_2 bubble is approximately equal to 0.07. The corresponding SP and second-order CG images (Figure 1b, c) exhibit high contrast over the bubble region. In Figure 1b, the SP value is defined as $(\varphi_S - \varphi_{tip})/e$ in the flat region (φ_S and φ_{tip} represent the work functions of the sample and the FM-KPFM tip), with more measurement details provided in Methods. In the bubble region, consistent with previous reports,[26,27,43] we observed evidence of a strain-induced piezoelectric field that exists from the edge to the center of bubbles, revealing the halo-like feature around the bubble edge region. The experimental statistics show that the SP of the bubble edge region is significantly higher than that of the bubble top region; this is due to the breaking of inversion symmetry in the intrinsic monolayer WS_2 and the presence of radial tensile stress in the bubble; the W−S dipole exhibits a nonzero polarization, leading to a redistribution of surface charge density and the corresponding built-in electric field along the radial direction of the bubbles, termed the piezoelectric field. Electrons were accumulated at the bubble top region, making the SP of the bubble top region to be lower than that of the bubble edge region. Here, for the bubble region, altering SP is described as $V_{SP} = (\varphi_S - \varphi_{tip})/e + EpdR$, where Ep denotes the polarization field and dR represents the differentiation of radial coordinates on bubble positions. It is worth noting that in Figure 1d, an SP deviation near the bubble edge region can be observed. In order to obtain more effective evidence on the electrical properties of the bubble and to rule out the influence of the dielectric environment on SP distribution, we chose to use a capacitive microscopy to measure the capacitance between the metallic tip and back electrode by a capacitance sensor connected to a built-in LCR meter.[44,45] The second derivative of capacitance (C) with respect to the tip−sample distance (z), i.e., $\partial^2C/\partial z^2$, referred as second-order CG mentioned above, is used to qualitatively monitor the spatial variation of capacitance which is proportional to the dielectric coefficient (see Supporting Note1 in Supporting Information (SI) for details). We measured the second-order CG on the WS_2 bubble which was shown in Figure 1c and found that the contrast characteristics were akin to those of the SP distribution. However, the second-order CG cross-sectional profile shows the region with the largest dielectric coefficient does not coincide with the position of halo-like in SP mapping in Figure 1d. The evidence effectively demonstrates that the halo-like feature in the SP mapping is not caused by the dielectric environment but rather by the presence of a piezoelectric field within the bubble. Moreover, the existence of the piezoelectric field is also verified by quantization calculation. When the stress field σ_{11} was subjected, piezoelectric field E was generated in monolayer WS_2. According to the piezoelectric tensor formula:

$$e_{11} = \frac{\partial\sigma_{11}}{\partial E_1} \tag{1}$$

the obtained piezoelectric coefficient is about 2.82 × 10^{-10} C m^{-1}, which accords well with that from theoretical calculations

https://doi.org/10.1021/acsami.4c00092
ACS Appl. Mater. Interfaces 2024, 16, 36735−36744

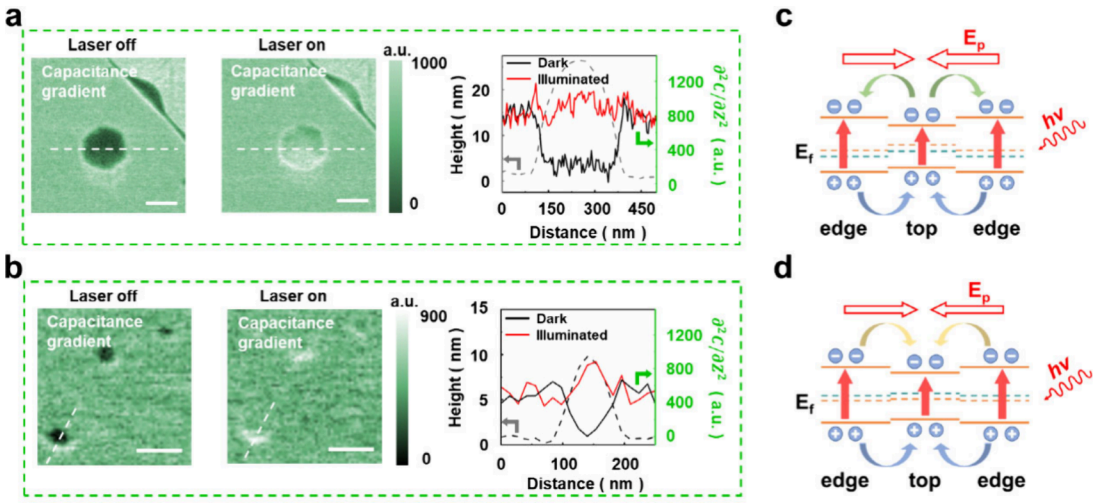

Figure 3. Comparison of second-order CG variations w/o and with illumination of the monolayer WS_2 bubbles on monolayer graphene. (a, b) Capacitance gradient measurements of the large WS_2 bubbles (a) and the pocket ones (b) on monolayer graphene, respectively. Profile of height, $\partial^2C/\partial z^2$ w/o and with illumination along the white dashed lines in Figure 2a, b, in the left and middle panels of (a, b), respectively. (c, d) Schematic diagram of the charge transfer and induced Fermi energy level shift of the bubble's top and edge area with illumination of large monolayer WS_2 bubbles for (c) and pocket ones for (d) on monolayer graphene. The orange E_f dashed line and green E_f dashed line represent the Fermi level without and with illumination, respectively. All scale bars, 200 nm. The pixel size is 3.89 × 3.89 nm^2 for the large WS_2/graphene bubbles (a) and 11.68 × 11.68 nm^2 for the pocket ones (b). The laser power is 0.2 mW.

(2.2×10^{-10} C m^{-1}).[39] The deviation between the experimental value and the theoretical value may be due to the nonuniform strain on the bubble in the experiment, while the theory usually assumes uniform strain.

Above, we demonstrated the strain-induced characteristic piezoelectricity in monolayer WS_2. Owing to the existence of the piezoelectric potential of monolayer WS_2, the maximum potential difference between the bubble region and the flat region is approximately 150 mV with illumination (see Figure S1), indicating a relatively narrow photogenerated voltage window that falls short of practical requirements for optoelectronic device. To align more with the practical application of optoelectronic devices, two fundamental issues must be addressed. First, it is crucial to enlarge the photoinduced voltage window, i.e., to maximize the potential difference between the bubble region and the flat region in our system as much as possible. Second, the bubble morphology could serve as a novel parameter, ensuring a deeper comprehension and effective control of the separation of the photogenerated electron−hole pair.

For this intent, monolayer graphene was integrated between the monolayer WS_2 and SiO_2/Si, forming a WS_2/graphene vdW heterojunction (see the Methods). In our WS_2/graphene heterostructures bubble system, the majority of bubbles present h/R values around 0.14. A subset of bubbles displays lower values, which could be due to the strain release of the one-dimensional structure, the probe convolution effect, or statistical errors caused by irregular shape. To confirm the precise localization of the bubbles, we deliberately avoided the formation of bubbles under the graphene layer during the dry-transfer process. The selection of graphene as the substrate in our study is motivated by its high lipophilicity and self-cleaning properties, which support the formation of relatively stable regular bubbles.[35−38] Figure 2 presents the results obtained for the monolayer WS_2 bubbles on monolayer graphene observed by FM-KPFM with or without illumination. Here, this study selects two representative bubbles with h/R values of 0.14 but varying h for comparative analysis. Figure 2a, b showed the AFM topography of the large bubble and the pocket bubble (see Figure S2 for 3D images of the two bubbles). 0.139 and 0.136 were obtained for the large bubbles and the pocket bubbles, respectively (Figure S3). First, it should be clarified that both bubble topographies remained relatively unchanged w/o and with illumination, maintaining a Gaussian distribution throughout,[46] and thus eliminating any topography changes induced by illumination or potential alterations in SP distribution. We present the SP distribution mappings and the corresponding cross-sectional SP profiles of the large and pocket bubbles without and with illumination (Figure 2c, d). It is worth noting that the changes in the flat region around the WS_2 bubbles tend to be consistent with illumination, and the potential decreases by nearly 200 mV. The decrease in potential within the flat region can be readily understood due to the graphene substrate beneath WS_2, as the self-cleaning effect prevents any doping for monolayer WS_2 by trapping gases or organic substances, thereby highlighting the pronounced influence of graphene. And to avert the WS_2/graphene interlayer charge transfer effect to the intrinsic piezoelectric properties of WS_2 nanobubbles, we constructed a contrast experiment of WS_2 nanobubbles on hBN, consistent with our experiment results (Figure S10). Meanwhile, more significantly, previous reports[35−38] have indicated that the relative alignment of WS_2 and graphene bands results in variations in the scattering phase space for electrons and holes. As a result, resonating with the A-exciton in WS_2 after photoexcitation, photogenerated holes are swiftly transferred to the graphene layer while photogenerated electrons remain in the WS_2 layer, which leads to a decrease in potential of the WS_2 layer (Figure S4). Interestingly, different from the relatively similar SP changes in the flat region, the two bubbles show opposite phenomena in the bubble region. The SP distribution mapping of the large bubble exhibits a distinct halo-like feature; meanwhile, the SP profile explicitly reveals the mutation region induced by the piezoelectric field, along with a prominent peak around the edge of the bubble. Incorporating with the mappings and profiles of the SP

https://doi.org/10.1021/acsami.4c00092
ACS Appl. Mater. Interfaces 2024, 16, 36735−36744

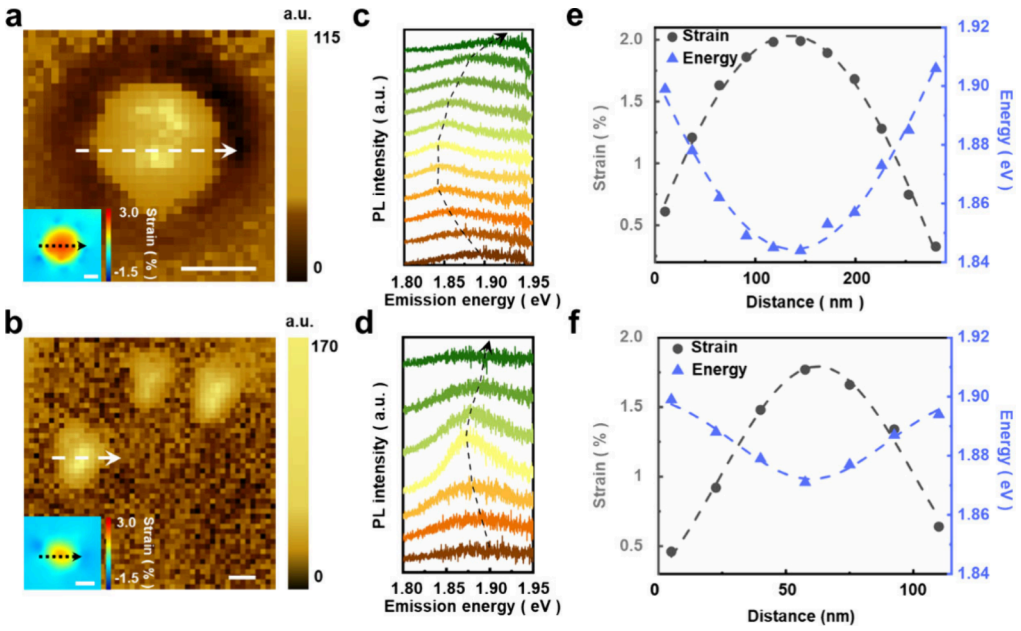

Figure 4. TEPL imaging of monolayer WS_2 /monolayer graphene system. (a, b) TEPL peak intensity images of a large (a) and pocket (b) bubble, integrated over the spectral range between 1.77 and 1.90 eV for (a) and between 1.83 and 1.93 eV for (b). Inset: Strain distribution images are for selected lined bubbles. The dashed lines in a, b represent the position and direction of the selected points. (c and d) TEPL spectra along the white dashed line in (a) panel a for (c) and in (b) panel for (d). The dashed lines in (c, d) correspond to the dashed lines in (a, b), respectively. (e, f) Strain and TEPL peak position along the black dashed line and white dashed line, respectively, in (a) for (e) and in (b) for (f). The dashed lines in (e, f) are the Gaussian fit for the relevant data. All scale bars are 100 nm. The pixel size is 10×10 nm^2 for the large WS_2/graphene bubbles (a) and 20×20 nm^2 for the pocket ones (b). The laser power is 0.2 mW.

distribution, we observed that SP of the large bubble region increased overall almost 90 mV with illumination (Figure 2c). Compared with the large bubbles, the halo-like feature of the pocket bubble is not readily discernible due to resolution limitations; however, piezoelectric-inductive inflection points in the SP profile can still be observed near the bubble edge region. The overall potential of the pocket bubble region decreased almost 70 mV (Figure 2d).

A significant augmentation in second-order CG values for both bubbles with illumination above our noise level have been recorded within the bubble zone in the corresponding second-order CG mappings, indicating charge accumulation within the bubble region (Figure 3a, b).[47−49] By analyzing the SP and second-order CG values variation within both bubble top regions (Figure S5), it is feasible to efficaciously discriminate different gathered carriers' categories with the complementary mixing of the two technologies.[50,51] According to the theoretical model deliberated previously, the piezoelectric field in the WS_2 bubble exhibits a directional orientation, from bubble edge toward top. The photogenerated electron−hole pair in the bubble region is separated by piezoelectric potentials with illumination, inciting carriers to migrate and accumulate along the potential gradient. Promoted by the piezoelectric field, the photogenerated holes should converge to the top region of the bubble, engendering the overall increase of SP, and the disparity between the maximum and minimum potentials in the bubble region diminishes. Associating with the experiments, the observation reveals that the large bubbles' phenomenon, which hole aggregation is the predominant photocarrier type within the bubble region with illumination, aligns with the proposition that carrier regulation is governed by the piezoelectric field, while the phenomenon in the pocket bubble regions exhibits a distinct contrast, manifested by electron accumulation unlike large bubbles, leading to an overall reduction in electric potential. Therefore, the electron−hole pairs separation dynamics process in the pocket bubble regions is believed to differ from the large bubble regions. We drew the schematic diagrams to graphically describe these two different photocarrier dynamic process in Figure 3c, d, respectively.[35−38] The green and yellow arrows represent different directions of carrier movement, while the thickness of the electric field arrows represents different sizes of the piezoelectric field strengths. The introduction of monolayer graphene substrate in our experiment successfully broadened the voltage window for the WS_2 bubbles, enabling a potential difference of approximately 500 mV between the bubble region and the surrounding flat region to gratify the effective voltage range for practical optoelectronic device applications.[52−54]

Although our WS_2/graphene bubble system overcomes the previous limitation of a narrow voltage window in simple WS_2 bubbles, we still encounter perplexity regarding the photogenerated carrier dynamics in bubbles with varying heights, particularly the phenomenon of electron aggregation within small bubbles remains unexplained by the piezoelectric field theoretical model.[27] With previous reports,[31−34] the existence of strain leads to the WS_2 bubble bending the energy band. Consequently, the valence band and conduction band of the bubble region are shifted to the higher energy level and the lower energy level respectively, known as the funneling effect.[31−34] The influence of the funneling effect on the photogenerated electron−hole cannot be neglected, as it induced a migration of photogenerated electrons and holes toward bubble central region, contributing to the SP. It should be emphasized that FM-KPFM attains the molecular average SP information but not reflects the relative shift of the valence

https://doi.org/10.1021/acsami.4c00092
ACS Appl. Mater. Interfaces 2024, 16, 36735−36744

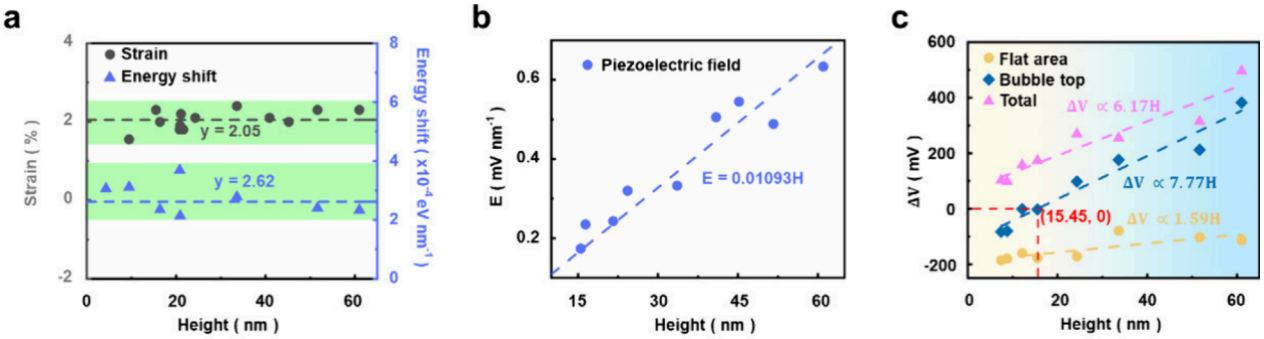

Figure 5. Effective manipulation of the localized properties by the monolayer WS_2 bubble's height on monolayer graphene system. (a) Correlation between the TEPL peak energy shift, the maximum strain and the height of the monolayer WS_2 bubbles on monolayer graphene. Blue- and gray dashed lines represent the fitting curve. The value of strain and TEPL energy shift values with different bubble's heights only fluctuate slightly within the fixed range. (b) Correlation between the strength of piezoelectric field and the height of the monolayer WS_2 bubbles on monolayer graphene. The blue dashed line is the linear fitting curve. (c) Correlation between the SP difference w/o and with illumination and the height of the monolayer WS_2 bubble on monolayer graphene, at the flat area (ΔV_{flat}), the bubble top (ΔV_{bubble_top}), and the total difference ($\Delta V_{total} = \Delta V_{bubble\_top} - \Delta V_{flat}$). The tan, blue, and purple dashed lines are the linear fitting curve. For the bubble top, (15.45, 0) is observed as a symbolic critical threshold point of ΔV_{bubble_top}.

band and conduction band, rendering it unpractical to divide the respective effects of funneling and piezoelectric fields on carrier motion. To solve this issue, FM-KPFM and TEPL spectroscopy were merged to obtain piezoelectric potential and illuminance mapping signals simultaneously *in situ*.[55−58] TEPL provokes a localized electromagnetic field boost by leveraging the plasmonic resonance on the gold metal tip and the lightning rod effect at the tiny tip-based junction.[59] In contrast to far-field (FF) PL, TEPL upholds exceptional sensitivity and spatial resolution down to 20 nm, enabling nanoscale detection.[60] The high-resolution TEPL mappings were both harvested by the full emission range, which are shown in Figure 4a, b, for the large bubble and the pocket bubble, respectively. More spatial mapping of the TEPL peak intensity of the two bubbles is shown in Figure S6 and S7. All mapping images were corrected by subtracting FF to exclude invalid stray signals (near-field PL (NF)-FF = TEPL), thereby landing more precise localized information (see the measurement details in the Methods). The insets of Figure 4a, b display the trace of the strain tensor for the two bubbles, which was calculated using the Föppl−von Kármán equation (see Supporting Note 2 in SI).[61] The strain distribution simulation clarifies that the maximum strains in bubbles are chiefly located at their centers, owing to slight irregularities in shape, there may be a minor deflection away from the center. However, the strain maximums and strain distributions of the two bubbles are coincident, corresponding to the neighboring h/R values in the identical system by previous studies.[42] To inspect the PL peak position variations, the PL spectrum along the white dashed lines across the bubble is depicted in Figure 4c, d, respectively. The characteristic peaks are discovered to exhibit a steady redshift from the bubble edge toward center. But in the flat region, on account of the interlayer carrier transfer, the excitons are quenched, so the PL signal cannot be probed.[62−64] The enormous strain of nanobubbles critically alters the optical bandgap and exciton PL energies by several tens of millielectronvolts. The band shift established by the strain-induced exciton funneling effect causes the overall carriers to tend to move toward the bubble top region, which is universal in our bubbles, regardless of bubble height. Figure 4e, f, demonstrates the strain and emission energy of the large bubble and pocket bubble versus the position, respectively. Through contrasting each other, the spatial variation of PL peak energy is accordant with the estimated maximum strain, both obeying Gaussian distribution.

Furthermore, we counted the maximum strain value and unit energy shift corresponding to the WS_2/graphene bubbles with various heights (Figure 5a). It is evident that these two parameters exhibit minimal variation for diverse bubble heights, near a stationary value. Specifically, the strain and the unit energy shift are approximately 2.05%, and 2.62×10^{-4} eV nm^{-1}, respectively. Therefore, through intuitive graphic presentation and comprehensive data statistics, we can essentially derive the following conclusions: the bubble heights in the identical system do not impact the disparity in band bending aroused by the funneling effect, as they possess coincident shapes and approximate strain distributions, i.e., h/R. Then deducing legitimately, when subjected to laser excitation, the aggregation of excitons in the bobble top region on account of the funneling effect also exhibits a similar phenomenon, echoing with a consistent energy displacement per unit length. For the funneling effect, the discrepancy of the valence band shift and conduction band shift under strain may evoke the imbalance of photocarrier aggregation in the bubble top region, more photoelectrons gathering, diminishing the SP ultimately. Related to earlier discussion, the SP distribution in the bubble region of large and pocket bubbles shows an opposite trend w/o and with illumination, and there may be a competitive relationship between the funneling effect and the piezoelectric field for the contribution to SP variation with illumination. Due to the funneling effect and the interlayer diffusion of WS_2/graphene heterojunction, the photogenerated electrons display a tendency to migrate toward the bubble top region, lowering the SP. This hypothesis aligns faultlessly with the unusual observation of SP distribution within the pocket bubble regions. Considering coexistence of the piezoelectric field, funneling filed and graphene diffusion, it is postulated that the larger bubble would possess a greater piezoelectric field compared to the pocket bubble, the overall SP of the larger bubble region is raised with illumination, surpassing the potential reduction caused by the funneling effect and the interlayer carrier transfer. As a corroboration, piezoelectric field strength of several bubbles was counted (Figure 5b), A linear augment was visualized, as denoted by $E = 0.01093H$, thereby

https://doi.org/10.1021/acsami.4c00092
ACS Appl. Mater. Interfaces 2024, 16, 36735−36744

corroborating our initial hypothesis, see Supporting Note 3 in SI for details, and then, the piezoelectric field distribution curve of the two bubbles were also obtained (Figure S8). Taking into account the laser power, we derived the correlation between the photoresponse and the different bubble heights (Figure S9). Then we can observe a nearly linear increase in photoresponse as the height of the bubble increases.

Finally, we calculate the SP variations in the bubble top region (average SP), flat region, and the total difference (subtracting the former two values from each other) of WS_2/graphene bubbles with different heights w/o and with illumination (Figure 5c). Upon observing a linear increase in all three variables, it was noted that the potential difference in the bubble region exhibited an upward trend with increasing bubble height w/o and with illumination. However, compared to the changes in the bubble region, the alterations in the flat region were relatively inconspicuous, likely due to the determined interlayer carrier transfer behavior. With the increase of the bubble's height, the electron diffusion effect caused by the interlayer carrier transfer also decreases. This reduction might be associated with the tiny range of winkles that appear at the edge of the large bubble. When the bubble height is about 15.45 nm, the potential of the bubble region changes to 0 mV w/o and with illumination, illustrating that 15.45 nm is a critical threshold.

CONCLUSIONS

In summary, combining unique *in situ* techniques, we have revealed the synergistic enhancement and competitive interplay of the piezoelectric effect, funneling effect, and interlayer carrier transfer on photogenerated electron−hole pairs dynamics in monolayer WS_2/monolayer graphene nanobubbles with varying heights. The piezoelectric field in the monolayer WS_2 nonheterojunction bubble system was visualized using FM-KPFM, verified by the representative halo-like features and the piezoelectric coefficient 2.82×10^{-10} C m^{-1} of the monolayer WS_2 obtained from the experiments, which accord well with that from theoretical calculations. By constructing monolayer WS_2/monolayer graphene heterojunction system, an exhilarating 3-fold enhancement was achieved in the photogenerated voltage window compared with the monolayer WS_2 bubble system with illumination. In addition, contrary to the large bubble region, the SP of the pocket bubble region diminished, and the electrons gathered with illumination, inexplicable by the conventional piezoelectric field theory. Utilizing *in situ* nanoscale TEPL technology, we found that the height of bubbles within the same system does not affect the band curvature per unit length caused by the funneling effect, however, the strain-induced piezoelectric field decreases linearly with reducing bubble height. When the bubble height is 15.45 nm, the piezoelectric effect, the interlayer carrier transfer, and the funneling effect cancel each other to achieve a balance. Combined with this discovery, different bubble sizes can be customized at specific locations on different substrates according to the application demands. Furthermore, considering its universality in TMDCs materials with inversion symmetry breaking, it is prosperous to assemble diverse categories of TMDCs materials for solar light harvesting and optical quantum information processing.

ASSOCIATED CONTENT

Supporting Information

The Supporting Information is available free of charge at https://pubs.acs.org/doi/10.1021/acsami.4c00092.

Topography and electrical characterization of monolayer WS_2 bubbles on Si/SiO_2 substrate with illumination, three-dimensional images and profiles of the large and pocket monolayer WS_2 bubbles, comparison of surface potential variations w/o and with illumination of monolayer WS_2 bubbles on hBN, Schematic diagram of the charge transfer and the induced Fermi energy level shift of the vertical WS_2/graphene heterojunction with illumination, height, the total SP difference ΔVtotal and $\partial^2 C/\partial z^2$ profile w/o illumination of the large and pocket monolayer WS_2 bubbles, spatial mapping of the TEPL peak intensity of the large and pocket monolayer WS_2 bubbles, comparison of electrical field images w/o and with illumination of the large and pocket monolayer WS_2 bubbles, the relationship between the photoresponse of the bubbles with the bubble's height, introduction of FM-KPFM mode, calculation of the bubbles' strain distributions, and the calculation of piezoelectric coefficient (PDF)

AUTHOR INFORMATION

Corresponding Authors

Shen Hu − *School of Microelectronics, Fudan University, Shanghai 200433, China; Jiashan Fudan Institute, Jiaxing 314110, China;* orcid.org/0000-0001-8162-1519; Email: hushen@fudan.edu.cn

Xuefeng Wu − *School of Microelectronics, Fudan University, Shanghai 200433, China; Shanghai Integrated Circuit Manufacturing Innovation Center, Shanghai 201210, China;* orcid.org/0000-0002-9672-6804; Email: xuefeng.wu@shnicic.com

Edward T. Yu − *Microelectronic Research Center, Department of Electrical and Computer Engineering, The University of Texas at Austin, Austin 78758, United States*; Email: ety@ece.utexas.edu

Li Ji − *School of Microelectronics, Fudan University, Shanghai 200433, China; Shanghai Integrated Circuit Manufacturing Innovation Center, Shanghai 201210, China; Jiashan Fudan Institute, Jiaxing 314110, China; Hubei Yangtze Memory Laboratories, Wuhan 430205, China;* orcid.org/0000-0002-2004-230X; Email: lji@fudan.edu.cn

Authors

Sheng Han − *School of Microelectronics, Fudan University, Shanghai 200433, China*

Jiong Liu − *School of Microelectronics, Fudan University, Shanghai 200433, China*

Ana I. Pérez-Jiménez − *Technology Innovation Institute, 9639 Abu Dhabi, United Arab Emirates*

Zhou Lei − *School of Microelectronics, Fudan University, Shanghai 200433, China*

Pei Yan − *School of Microelectronics, Fudan University, Shanghai 200433, China*

Yu Zhang − *School of Microelectronics, Fudan University, Shanghai 200433, China*

Xiangyu Guo − *School of Microelectronics, Fudan University, Shanghai 200433, China*

https://doi.org/10.1021/acsami.4c00092
ACS Appl. Mater. Interfaces 2024, 16, 36735−36744

Rongxu Bai − *School of Microelectronics, Fudan University, Shanghai 200433, China*
David W. Zhang − *School of Microelectronics, Fudan University, Shanghai 200433, China; Shanghai Integrated Circuit Manufacturing Innovation Center, Shanghai 201210, China; Jiashan Fudan Institute, Jiaxing 314110, China; Hubei Yangtze Memory Laboratories, Wuhan 430205, China*
Qingqing Sun − *School of Microelectronics, Fudan University, Shanghai 200433, China; Shanghai Integrated Circuit Manufacturing Innovation Center, Shanghai 201210, China; Jiashan Fudan Institute, Jiaxing 314110, China;* orcid.org/0000-0002-6533-1834
Deji Akinwande − *Microelectronic Research Center, Department of Electrical and Computer Engineering, The University of Texas at Austin, Austin 78758, United States;* orcid.org/0000-0001-7133-5586

Complete contact information is available at: https://pubs.acs.org/10.1021/acsami.4c00092

Author Contributions

¶S.H. and J.L. contributed equally to this work.

Notes

The authors declare no competing financial interest.

■ ACKNOWLEDGMENTS

This work is partially supported by the NSFC (62004044; 62204048), and by State Key Laboratory of ASIC & System (2021MS004). E.T.Y. acknowledges support from the U.S. National Science Foundation through grant no. CBET-2109842.

■ REFERENCES

(1) Ma, Q.; Ren, G.; Xu, K.; Ou, J. Z. Tunable Optical Properties of 2D Materials and Their Applications. *Adv. Opt. Mater.* **2021**, *9*, No. 2001313.
(2) Palacios-Berraquero, C.; Kara, D. M.; Montblanch, A. R. P.; Barbone, M.; Latawiec, P.; Yoon, D.; Ott, A. K.; Loncar, M.; Ferrari, A. C.; Atatüre, M. Large-Scale Quantum-Emitter Arrays in Atomically Thin Semiconductors. *Nat. Commun.* **2017**, *8*, 15093.
(3) Gu, J.; Chakraborty, B.; Khatoniar, M.; Menon, V. M. A Room-Temperature Polariton Light-Emitting Diode Based on Monolayer WS_2. *Nat. Nanotechnol.* **2019**, *14*, 1024−1028.
(4) Li, Z.; Xu, B.; Liang, D.; Pan, A. Polarization-Dependent Optical Properties and Optoelectronic Devices of 2D Materials. *Research* **2020**, *2020*, No. 5464258.
(5) Bie, Y.-Q.; Grosso, G.; Heuck, M.; Furchi, M. M.; Cao, Y.; Zheng, J.; Bunandar, D.; Navarro-Moratalla, E.; Zhou, L.; Efetov, D. K.; Taniguchi, T.; Watanabe, K.; Kong, J.; Englund, D.; Jarillo-Herrero, P. A $MoTe_2$-Based Light-Emitting Diode and Photodetector for Silicon Photonic Integrated Circuits. *Nat. Nanotechnol.* **2017**, *12*, 1124−1129.
(6) Kim, K. S.; Ji, Y. J.; Kim, K. H.; Choi, S.; Kang, D.-H.; Heo, K.; Cho, S.; Yim, S.; Lee, S.; Park, J.-H.; Jung, Y. S.; Yeom, G. Y. Ultrasensitive MoS_2 Photodetector by Serial Nano-Bridge Multi-Heterojunction. *Nat. Commun.* **2019**, *10*, 4701.
(7) Yang, H.; Wang, Y.; Zou, X.; Bai, R.; Wu, Z.; Han, S.; Chen, T.; Hu, S.; Zhu, H.; Chen, L.; et al. Wafer-Scale Synthesis of WS_2 Films with in Situ Controllable P-Type Doping by Atomic Layer Deposition. *Research* **2021**, *2021*, No. 7863483.
(8) Duan, R.; Qi, W.; Li, P.; Tang, K.; Ru, G.; Liu, W. A High-Performance MoS_2-Based Visible−near-Infrared Photodetector from Gateless Photogating Effect Induced by Nickel Nanoparticles. *Research* **2023**, *6*, No. 0195.
(9) Fan, F. R.; Wu, W. Emerging Devices Based on Two-Dimensional Monolayer Materials for Energy Harvesting. *Research* **2019**, *2019*, No. 7367828.
(10) Liang, M.; Ali, A.; Belaidi, A.; Hossain, M. I.; Ronan, O.; Downing, C.; Tabet, N.; Sanvito, S.; Ei-Mellouhi, F.; Nicolosi, V. Improving Stability of Organometallic-Halide Perovskite Solar Cells Using Exfoliation Two-Dimensional Molybdenum Chalcogenides. *npj 2D Mater. Appl.* **2020**, *4*, 40.
(11) Nassiri Nazif, K.; Daus, A.; Hong, J.; Lee, N.; Vaziri, S.; Kumar, A.; Nitta, F.; Chen, M. E.; Kananian, S.; Islam, R.; Kim, K.-H.; Park, J.-H.; Poon, A. S. Y.; Brongersma, M. L.; Pop, E.; Saraswat, K. C. High-Specific-Power Flexible Transition Metal Dichalcogenide Solar Cells. *Nat. Commun.* **2021**, *12*, 7034.
(12) Mahler, B.; Hoepfner, V.; Liao, K.; Ozin, G. A. Colloidal Synthesis of 1T-WS_2 and 2H-WS_2 Nanosheets: Applications for Photocatalytic Hydrogen Evolution. *J. Am. Chem. Soc.* **2014**, *136*, 14121−14127.
(13) Parzinger, E.; Miller, B.; Blaschke, B.; Garrido, J. A.; Ager, J. W.; Holleitner, A.; Wurstbauer, U. Photocatalytic Stability of Single- and Few-Layer MoS_2. *ACS Nano* **2015**, *9*, 11302−11309.
(14) Bao, X.; Ou, Q.; Xu, Z.-Q.; Zhang, Y.; Bao, Q.; Zhang, H. Band Structure Engineering in 2D Materials for Optoelectronic Applications. *Adv. Mater. Technol.* **2018**, *3*, No. 1800072.
(15) Ye, K.; Liu, L.; Liu, Y.; Nie, A.; Zhai, K.; Xiang, J.; Wang, B.; Wen, F.; Mu, C.; Zhao, Z.; et al. Lateral Bilayer MoS_2−WS_2 Heterostructure Photodetectors with High Responsivity and Detectivity. *Adv. Opt. Mater.* **2019**, *7*, No. 1900815.
(16) Fang, F.; Wan, Y.; Li, H.; Fang, S.; Huang, F.; Zhou, B.; Jiang, K.; Tung, V.; Li, L.-J.; Shi, Y. Two-Dimensional $Cs_2AgBiBr_6$/WS_2 Heterostructure-Based Photodetector with Boosted Detectivity Via Interfacial Engineering. *ACS Nano* **2022**, *16*, 3985−3993.
(17) Wu, D.; Guo, J.; Wang, C.; Ren, X.; Chen, Y.; Lin, P.; Zeng, L.; Shi, Z.; Li, X. J.; Shan, C.-X.; et al. Ultrabroadband and High-Detectivity Photodetector Based on WS_2/Ge Heterojunction through Defect Engineering and Interface Passivation. *ACS Nano* **2021**, *15*, 10119−10129.
(18) Li, J.; Bai, J.; Meng, M.; Hu, C.; Yuan, H.; Zhang, Y.; Sun, L. Improved Temporal Response of MoS_2 Photodetectors by Mild Oxygen Plasma Treatment. *Nanomaterials* **2022**, *12*, 1365.
(19) Jiang, J.; Xu, T.; Lu, J.; Sun, L.; Ni, Z. Defect Engineering in 2D Materials: Precise Manipulation and Improved Functionalities. *Research* **2019**, *2019*, 4641739.
(20) Gant, P.; Huang, P.; Perez de Lara, D.; Guo, D.; Frisenda, R.; Castellanos-Gomez, A. A Strain Tunable Single-Layer MoS_2 Photodetector. *Mater. Today* **2019**, *27*, 8−13.
(21) Mao, J.; Wu, Z.; Guo, F.; Hao, J. Strain-Induced Performance Enhancement of a Monolayer Photodetector Via Patterned Substrate Engineering. *ACS Appl. Mater. Interfaces* **2022**, *14*, 36052−36059.
(22) Feng, J.; Qian, X.; Huang, C.-W.; Li, J. Strain-Engineered Artificial Atom as a Broad-Spectrum Solar Energy Funnel. *Nat. Photonics* **2012**, *6*, 866−872.
(23) Desai, S. B.; Seol, G.; Kang, J. S.; Fang, H.; Battaglia, C.; Kapadia, R.; Ager, J. W.; Guo, J.; Javey, A. Strain-Induced Indirect to Direct Bandgap Transition in Multilayer WSe_2. *Nano Lett.* **2014**, *14*, 4592−4597.
(24) Lloyd, D.; Liu, X.; Christopher, J. W.; Cantley, L.; Wadehra, A.; Kim, B. L.; Goldberg, B. B.; Swan, A. K.; Bunch, J. S. Band Gap Engineering with Ultralarge Biaxial Strains in Suspended Monolayer MoS_2. *Nano Lett.* **2016**, *16*, 5836−5841.
(25) Hasz, K.; Hu, Z.; Park, K.-D.; Raschke, M. B. Tip-Enhanced Dark Exciton Nanoimaging and Local Strain Control in Monolayer WSe_2. *Nano Lett.* **2023**, *23*, 198−204.
(26) Ares, P.; Cea, T.; Holwill, M.; Wang, Y. B.; Roldán, R.; Guinea, F.; Andreeva, D. V.; Fumagalli, L.; Novoselov, K. S.; Woods, C. R. Piezoelectricity in Monolayer Hexagonal Boron Nitride. *Adv. Mater.* **2020**, *32*, No. 1905504.
(27) Wang, W.; Zhou, L.; Hu, S.; Novoselov, K. S.; Cao, Y. Visualizing Piezoelectricity on 2D Crystals Nanobubbles. *Adv. Funct. Mater.* **2021**, *31*, No. 2005053.

(28) Brennan, C. J.; Ghosh, R.; Koul, K.; Banerjee, S. K.; Lu, N.; Yu, E. T. Out-of-Plane Electromechanical Response of Monolayer Molybdenum Disulfide Measured by Piezoresponse Force Microscopy. *Nano Lett.* **2017**, *17*, 5464−5471.
(29) Brennan, C. J.; Koul, K.; Lu, N.; Yu, E. T. Out-of-Plane Electromechanical Coupling in Transition Metal Dichalcogenides. *Appl. Phys. Lett.* **2020**, *116*, No. 053101.
(30) Khan, A. R.; Lu, T.; Ma, W.; Lu, Y.; Liu, Y. Tunable Optoelectronic Properties of WS_2 by Local Strain Engineering and Folding. *Adv. Electron. Mater.* **2020**, *6*, No. 1901381.
(31) Lee, J.; Yun, S. J.; Seo, C.; Cho, K.; Kim, T. S.; An, G. H.; Kang, K.; Lee, H. S.; Kim, J. Switchable, Tunable, and Directable Exciton Funneling in Periodically Wrinkled WS_2. *Nano Lett.* **2021**, *21*, 43−50.
(32) Conley, H. J.; Wang, B.; Ziegler, J. I.; Haglund, R. F., Jr.; Pantelides, S. T.; Bolotin, K. I. Bandgap Engineering of Strained Monolayer and Bilayer MoS_2. *Nano Lett.* **2013**, *13*, 3626−3630.
(33) Castellanos-Gomez, A.; Roldán, R.; Cappelluti, E.; Buscema, M.; Guinea, F.; van der Zant, H. S. J.; Steele, G. A. Local Strain Engineering in Atomically Thin MoS_2. *Nano Lett.* **2013**, *13*, 5361−5366.
(34) Mangu, V. S.; Zamiri, M.; Brueck, S. R. J.; Cavallo, F. Strain Engineering, Efficient Excitonic Photoluminescence, and Exciton Funnelling in Unmodified MoS_2 Nanosheets. *Nanoscale* **2017**, *9*, 16602−16606.
(35) Aeschlimann, S.; Rossi, A.; Chávez-Cervantes, M.; Krause, R.; Arnoldi, B.; Stadtmüller, B.; Aeschlimann, M.; Forti, S.; Fabbri, F.; Coletti, C.; Gierz, I. Direct Evidence for Efficient Ultrafast Charge Separation in Epitaxial WS_2/Graphene Heterostructures. *Sci. Adv.* **2020**, *6*, No. eaay0761.
(36) Yuan, L.; Chung, T.-F.; Kuc, A.; Wan, Y.; Xu, Y.; Chen, Y. P.; Heine, T.; Huang, L. Photocarrier Generation from Interlayer Charge-Transfer Transitions in WS_2-Graphene Heterostructures. *Sci. Adv.* **2018**, *4*, No. e1700324.
(37) Fu, S.; du Fossé, I.; Jia, X.; Xu, J.; Yu, X.; Zhang, H.; Zheng, W.; Krasel, S.; Chen, Z.; Wang, Z. M.; Tielrooij, K.; Bonn, M.; Houtepen, A.; Wang, H. Long-Lived Charge Separation Following Pump-Wavelength−Dependent Ultrafast Charge Transfer in Graphene/WS_2 Heterostructures. *Sci. Adv.* **2021**, *7*, No. eabd9061.
(38) Krause, R.; Aeschlimann, S.; Chávez-Cervantes, M.; Perea-Causin, R.; Brem, S.; Malic, E.; Forti, S.; Fabbri, F.; Coletti, C.; Gierz, I. Microscopic Understanding of Ultrafast Charge Transfer in Van Der Waals Heterostructures. *Phys. Rev. Lett.* **2021**, *127*, No. 276401.
(39) Duerloo, K.-A. N.; Ong, M. T.; Reed, E. J. Intrinsic Piezoelectricity in Two-Dimensional Materials. *J. Phys. Chem. Lett.* **2012**, *3*, 2871−2876.
(40) Khestanova, E.; Guinea, F.; Fumagalli, L.; Geim, A. K.; Grigorieva, I. V. Universal Shape and Pressure inside Bubbles Appearing in Van Der Waals Heterostructures. *Nat. Commun.* **2016**, *7*, 12587.
(41) Dai, Z.; Hou, Y.; Sanchez, D. A.; Wang, G.; Brennan, C. J.; Zhang, Z.; Liu, L.; Lu, N. Interface-Governed Deformation of Nanobubbles and Nanotents Formed by Two-Dimensional Materials. *Phys. Rev. Lett.* **2018**, *121*, No. 266101.
(42) Tyurnina, A. V.; Bandurin, D. A.; Khestanova, E.; Kravets, V. G.; Koperski, M.; Guinea, F.; Grigorenko, A. N.; Geim, A. K.; Grigorieva, I. V. Strained Bubbles in Van Der Waals Heterostructures as Local Emitters of Photoluminescence with Adjustable Wavelength. *ACS Photonics* **2019**, *6*, 516−524.
(43) De Palma, A. C.; Peng, X.; Arash, S.; Gao, F. Y.; Baldini, E.; Li, X.; Yu, E. T. Elucidating Piezoelectricity and Strain in Monolayer MoS_2 at the Nanoscale Using Kelvin Probe Force Microscopy. *Nano Lett.* **2024**, *24*, 1835−1842.
(44) Riedel, C.; Arinero, R.; Tordjeman, P.; Ramonda, M.; Lévêque, G.; Schwartz, G. A.; Oteyza, D. G. d.; Alegria, A.; Colmenero, J. Determination of the Nanoscale Dielectric Constant by Means of a Double Pass Method Using Electrostatic Force Microscopy. *J. Appl. Phys.* **2009**, *106*, 024315.
(45) Lilliu, S.; Maragliano, C.; Hampton, M.; Elliott, M.; Stefancich, M.; Chiesa, M.; Dahlem, M. S.; Macdonald, J. E. Efm Data Mapped into 2D Images of Tip-Sample Contact Potential Difference and Capacitance Second Derivative. *Sci. Rep.* **2013**, *3*, 3352.
(46) Zhang, D.; Gan, L.; Zhang, J.; Zhang, R.; Wang, Z.; Feng, J.; Sun, H.; Ning, C.-Z. Reconstructing Local Profile of Exciton−Emission Wavelengths across a WS_2 Bubble Beyond the Diffraction Limit. *ACS Nano* **2020**, *14*, 6931−6937.
(47) Wu, D.; Pak, A. J.; Liu, Y.; Zhou, Y.; Wu, X.; Zhu, Y.; Lin, M.; Han, Y.; Ren, Y.; Peng, H.; Tsai, Y.; Hwang, G.; Lai, K. Thickness-Dependent Dielectric Constant of Few-Layer In_2Se_3 Nanoflakes. *Nano Lett.* **2015**, *15*, 8136−8140.
(48) Kang, Y.; Jeon, D.; Kim, T. Direct Observation of the Thickness-Dependent Dielectric Response of MoS_2 and WSe_2. *J. Phys. Chem. C* **2020**, *124*, 18316−18320.
(49) Kang, Y.; Jeon, D.; Kim, T. Local Mapping of the Thickness-Dependent Dielectric Constant of MoS_2. *J. Phys. Chem. C* **2021**, *125*, 3611−3615.
(50) Maragliano, C.; Lilliu, S.; Dahlem, M. S.; Chiesa, M.; Souier, T.; Stefancich, M. Quantifying Charge Carrier Concentration in Zno Thin Films by Scanning Kelvin Probe Microscopy. *Sci. Rep.* **2014**, *4*, 4203.
(51) Melios, C.; Panchal, V.; Giusca, C. E.; Strupiński, W.; Silva, S. R. P.; Kazakova, O. Carrier Type Inversion in Quasi-Free Standing Graphene: Studies of Local Electronic and Structural Properties. *Sci. Rep.* **2015**, *5*, 10505.
(52) Tsai, T.-H.; Sahoo, A. K.; Syu, H.-K.; Wu, Y.-C.; Tsai, M.-Y.; Siao, M.-D.; Yang, Y.-C.; Lin, Y.-F.; Liu, R.-S.; Chiu, P.-W. WS_2/WSe_2 Nanodot Composite Photodetectors for Fast and Sensitive Light Detection. *ACS Appl. Electron. Mater.* **2021**, *3*, 4291−4299.
(53) Namgung, S.; Shaver, J.; Oh, S.-H.; Koester, S. J. Multimodal Photodiode and Phototransistor Device Based on Two-Dimensional Materials. *ACS Nano* **2016**, *10*, 10500−10506.
(54) Yeh, C.-H.; Chen, H.-C.; Lin, H.-C.; Lin, Y.-C.; Liang, Z.-Y.; Chou, M.-Y.; Suenaga, K.; Chiu, P.-W. Ultrafast Monolayer In/Gr-WS_2-Gr Hybrid Photodetectors with High Gain. *ACS Nano* **2019**, *13*, 3269−3279.
(55) Lu, J.; Yao, J.; Yan, J.; Gao, W.; Huang, L.; Zheng, Z.; Zhang, M.; Li, J. Strain Engineering Coupled with Optical Regulation Towards a High-Sensitivity In_2S_3 Photodetector. *Mater. Horiz.* **2020**, *7*, 1427−1435.
(56) Xia, H.; Luo, M.; Wang, W.; Wang, H.; Li, T.; Wang, Z.; Xu, H.; Chen, Y.; Zhou, Y.; Wang, F.; Xie, R.; Wang, P.; Hu, W.; Lu, W. Pristine PN Junction toward Atomic Layer Devices. *Light Sci. Appl.* **2022**, *11*, 170.
(57) Park, K.-D.; Jiang, T.; Clark, G.; Xu, X.; Raschke, M. B. Radiative Control of Dark Excitons at Room Temperature by Nano-Optical Antenna-Tip Purcell Effect. *Nat. Nanotechnol.* **2018**, *13*, 59−64.
(58) Lamsaadi, H.; Beret, D.; Paradisanos, I.; Renucci, P.; Lagarde, D.; Marie, X.; Urbaszek, B.; Gan, Z.; George, A.; Watanabe, K.; Taniguchi, T.; Turchanin, A.; Lombez, L.; Combe, N.; Paillard, V.; Poumirol, J. Kapitza-Resistance-Like Exciton Dynamics in Atomically Flat $MoSe_2$-WSe_2 Lateral Heterojunction. *Nat. Commun.* **2023**, *14*, 5881.
(59) Su, W.; Kumar, N.; Shu, H.; Lancry, O.; Chaigneau, M. In Situ Visualization of Optoelectronic Behavior of Grain Boundaries in Monolayer WSe_2 at the Nanoscale. *J. Phys. Chem. C* **2021**, *125*, 26883−26891.
(60) Darlington, T. P.; Carmesin, C.; Florian, M.; Yanev, E.; Ajayi, O.; Ardelean, J.; Rhodes, D. A.; Ghiotto, A.; Krayev, A.; Watanabe, K.; Taniguchi, T.; Kysar, J.; Pasupathy, A.; Hone, J.; Jahnke, F.; Borys, N.; Schuck, P. Imaging Strain-Localized Excitons in Nanoscale Bubbles of Monolayer WSe_2 at Room Temperature. *Nat. Nanotechnol.* **2020**, *15*, 854−860.
(61) Darlington, T. P.; Krayev, A.; Venkatesh, V.; Saxena, R.; Kysar, J. W.; Borys, N. J.; Jariwala, D.; Schuck, P. J. Facile and Quantitative Estimation of Strain in Nanobubbles with Arbitrary Symmetry in 2D Semiconductors Verified Using Hyperspectral Nano-Optical Imaging. *J. Chem. Phys.* **2020**, *153*, 024702.

https://doi.org/10.1021/acsami.4c00092
ACS Appl. Mater. Interfaces 2024, 16, 36735−36744

(62) Buscema, M.; Steele, G. A.; Van Der Zant, H. S.; Castellanos-Gomez, A. The Effect of the Substrate on the Raman and Photoluminescence Emission of Single-Layer MoS_2. *Nano Res.* **2014**, *7*, 561−571.
(63) Tran, M. D.; Kim, J.-H.; Lee, Y. H. Tailoring Photoluminescence of Monolayer Transition Metal Dichalcogenides. *Curr. Appl. Phys.* **2016**, *16*, 1159−1174.
(64) Froehlicher, G.; Lorchat, E.; Berciaud, S. Charge Versus Energy Transfer in Atomically Thin Graphene-Transition Metal Dichalcogenide Van Der Waals Heterostructures. *Phys. Rev. X* **2018**, *8*, No. 011007.

https://doi.org/10.1021/acsami.4c00092
ACS Appl. Mater. Interfaces 2024, 16, 36735−36744